electronic reprint

Diffraction and imaging study of imperfections of crystallized lysozyme with coherent X-rays

Z. W. Hu, Y. S. Chu, B. Lai, B. R. Thomas and A. A. Chernov

Diffraction and imaging study of imperfections of crystallized lysozyme with coherent X-rays

Z. W. Hu,[a]* Y. S. Chu,[b] B. Lai,[b]
B. R. Thomas[a] and
A. A. Chernov[a]

[a]BAE Systems, NASA/Marshall Space Flight
Center, Huntsville, AL 35812, USA, and
[b]Advanced Photon Source, Argonne National
Laboratory, Argonne, IL 60439, USA

Correspondence e-mail:
zhengwei.hu@msfc.nasa.gov

Phase-contrast X-ray diffraction imaging and high-angular-resolution diffraction combined with phase-contrast radiographic imaging were employed to characterize defects and perfection of a uniformly grown tetragonal lysozyme crystal in the symmetric Laue case. The full-width at half-maximum (FWHM) of a 4 4 0 rocking curve measured from the original crystal was ~16.7 arcsec and imperfections including line defects, inclusions and other microdefects were observed in the diffraction images of the crystal. The observed line defects carry distinct dislocation features running approximately along the $\langle 1\,1\,0 \rangle$ growth front and have been found to originate mostly in a central growth area and occasionally in outer growth regions. Inclusions of impurities or formations of foreign particles in the central growth region are resolved in the images with high sensitivity to defects. Slow dehydration led to the broadening of a fairly symmetric 4 4 0 rocking curve by a factor of ~2.6, which was primarily attributed to the dehydration-induced microscopic effects that are clearly shown in X-ray diffraction images. The details of the observed defects and the significant change in the revealed microstructures with drying provide insight into the nature of imperfections, nucleation and growth, and the properties of protein crystals.

1. Introduction

Characterization of defects in bulk protein and other biological macromolecular crystals by X-ray methods presents a greater challenge than in small-molecule crystals, although considerable progress has been made since the first X-ray topographic work on protein crystals (Fourme *et al.*, 1995). This arises partly from the fact that proteins are made up of low-Z atoms, such as H, C, N and O, which scatter X-rays weakly. The intrinsically weak scattering power of X-rays in protein crystals can give rise to difficulty in X-ray topographic visualization of defects and X-ray diffraction measurements of lattice mosaicity, although the low X-ray absorption means that the whole bulk of the crystals can be examined by transmission X-ray topography. Furthermore, protein crystals contain a high percentage of solvent varying from ~30 to 65% (Matthews, 1968) that defines most of the unique features of protein crystals (McPherson, 1998). Special care needs to be taken in handling protein samples in order to prevent the soft and fragile crystals from being damaged both mechanically and chemically prior to any serious measurements. This is particularly true for high-angular-resolution X-ray diffraction and imaging studies of crystal mosaicity and defects. Unless cryocooling is needed to avoid radiation damage (Garman & Schneider, 1997; Garman, 1999), protein crystals are normally mounted in X-ray capillaries in which crystals adhere to the

electronic reprint

capillary wall owing to the surface tension of the mother liquor between the crystal and the capillary wall. Because of the delicate nature of protein crystals, a slight disturbance to the local environment of the crystal may affect the system equilibrium and the status of the protein crystals. Indeed, the issue of dehydration-induced effects on the structures, physical properties and lattice order of protein crystals has long been a subject of interest (see, for example, Perutz, 1942; Blake *et al.*, 1983; Morozov *et al.*, 1985; Salunke *et al.*, 1985; Dobrianov *et al.*, 2001). However, thus far our understanding has been limited in how defects respond to dehydration and how they are affected by various forces. On the whole, questions remain in bulk protein crystals concerning the nature of defects and the origins of the formation of imperfections. Given that the bottleneck for structural determination of proteins by X-ray crystallography is the growth of highly perfect crystals or crystals with fewer defects and better lattice order (Chayen, 2002), it is of importance both scientifically and practically to map crystal imperfections and to understand how they are created by applying effective approaches.

Recently, it has recently been demonstrated that spatial coherence-based phase-sensitive or phase-contrast X-ray diffraction imaging (Hu *et al.*, 1998) can be highly sensitive to lattice deviations from perfection in protein crystals (Hu, Lai *et al.*, 2001) and has the potential to provide a solution to difficulties in the characterization of defects of bulk macromolecular crystals. In the present paper, we employ X-ray diffraction and phase-sensitive X-ray diffraction imaging techniques combined with phase-sensitive radiographic imaging for further examination of defects, in particular line defects of uniformly crystallized lysozyme and the effects of dehydration on crystal perfection, in some detail. We shall begin with a brief description of the major differences between small-molecule crystals and biological macromolecular crystals (from an X-ray scattering point of view) and the implication of these differences for X-ray characterization of protein crystals, followed by experimental details on X-ray diffraction and imaging measurements and crystal growth. The experimental results will then be discussed.

2. X-ray topography of protein crystals: a special case?

Conventional X-ray diffraction topography has high sensitivity to defects in small-molecule crystals that are made visible by either extinction contrast or orientation contrast or both (Lang, 1978; Tanner, 1976; Klapper, 1991; Authier, 2001). While the degree of lattice perfection is obviously an external factor influencing the intensity across the crystal, there are two important intrinsic parameters in X-ray diffraction topography that dictate sensitivity to structural imperfections: the extinction length of the reflection used and the intrinsic rocking-curve width of the reflection. It was realised by Helliwell (1988) that the intrinsic rocking-curve widths of a perfect protein crystal can be less than 1 arcsec from the dynamical theory of X-ray diffraction. In order to understand X-ray diffraction contrast, the diffraction features of X-rays in protein crystals have also been discussed to some extent in

papers published subsequently (*e.g.* Fourme *et al.*, 1995; Otalora *et al.*, 1999; Hu, Lai *et al.*, 2001; Vetter *et al.*, 2002). To simplify the description, we only consider symmetric transmission (the symmetric Laue case) that indeed is the case in the experiments shown below. Given that absorption is negligible for protein crystals, the intrinsic rocking-curve width or full-width at half-maximum (FWHM), $\theta_{1/2}$, is therefore given by

$$\theta_{1/2} = 2d\xi_g^{-1}, \tag{1}$$

where d is the interplanar spacing of the Bragg reflection concerned and ξ_g is the extinction length of the reflection whose diffraction vector is **g**. In the symmetric Laue case, ξ_g can be simplified as follows,

$$\xi_g = \frac{\pi \cos \theta_B}{Cr_e \lambda (F_g/V)}, \tag{2}$$

where r_e is the classical electron radius ($r_e = 2.82 \times 10^{-5}$ Å), F_g is the structure factor, V is the volume of the unit cell, C is the polarization factor ($C \simeq 1$ in our experiments), λ is the wavelength of X-ray radiation and θ_B is the Bragg angle.
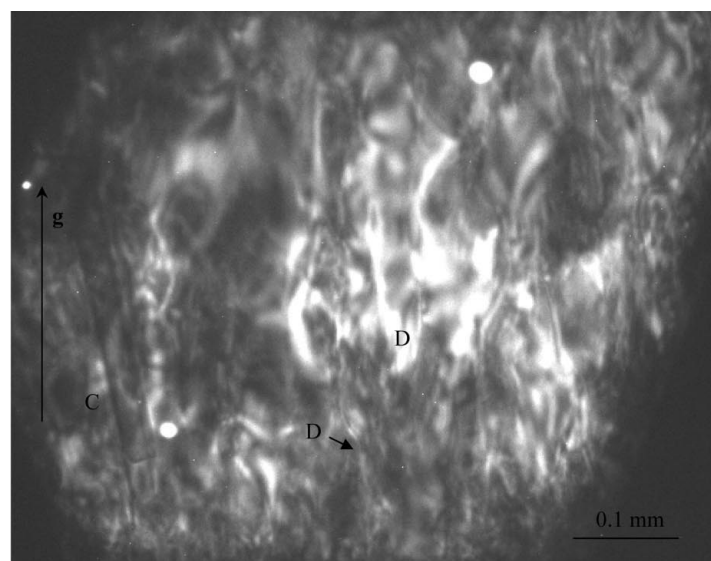
It is immediately clear from (2) that the extinction lengths for protein crystals can be far larger than those for most small-molecule crystals because of the extremely weak X-ray scattering power (F_g/V) of the former. Roughly speaking, the extinction length for a typical reflection at 1 Å radiation varies from millimetres to tens of millimetres or so in protein crystals, compared with a few micrometres to several tens of micrometres in most small-molecule crystals. For example, the extinction distance is approximately 1.9 mm for 4 4 0, a strong reflection of the tetragonal lysozyme form, and 5.3 mm for 26 0 2, a 3 Å diffraction-resolution reflection of the tetragonal lysozyme form with reasonable intensity (the theoretically estimated value is ~1412 for $F_{4\,4\,0}$ and ~489 for $F_{26\,0\,2}$ based on the structural data; Lim *et al.*, 1998). The large extinction lengths can make it difficult to obtain the direct image of dislocations in protein and other macromolecular crystals, a type of extinction contrast that is predominant in Lang X-ray topographs of small-molecule crystals. If the crystal thickness is less than ~0.25–0.3ξ_g, the dislocation contrast normally disappears (Tanner, 1976; Lang, 1978; Authier, 2001). Given the limited size (typically less than 0.5 mm in size) or rather the limited thickness of protein crystals, the extinction contrast of dislocations would in most cases probably be either weak or absent in conventional X-ray topographs. To maximize the probability of visualizing dislocations in terms of extinction contrast, we may have to invoke the strongest reflections, together with the use of extremely large crystals whose thickness is comparable to the extinction lengths of the reflections. Such a strategy may have been implicitly used in a study of a tetragonal lysozyme crystal by Laue topography (Izumi *et al.*, 1999). On the other hand, as is known, the dislocation-image widths in X-ray topographs of inorganic crystals are normally several micrometres or slightly more, *i.e.* of the order of the extinction lengths of the reflections used. We have yet to ascertain whether or not the long extinction
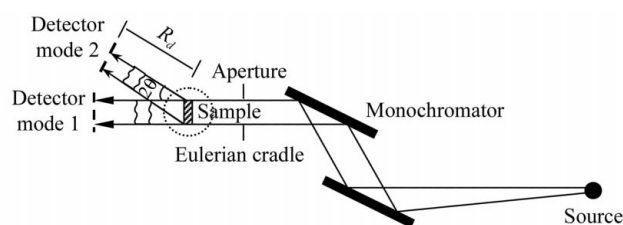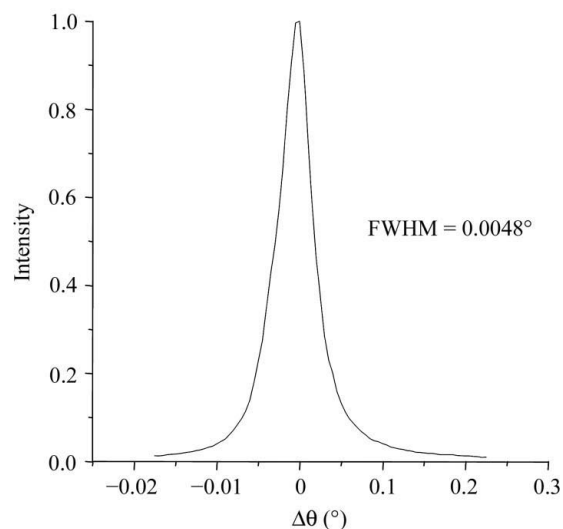
Figure 1
Schematic drawing of the experimental setup for phase-sensitive X-ray imaging and diffraction.

lengths of protein crystals would cause a problem in resolving dislocations from the extinction contrast.
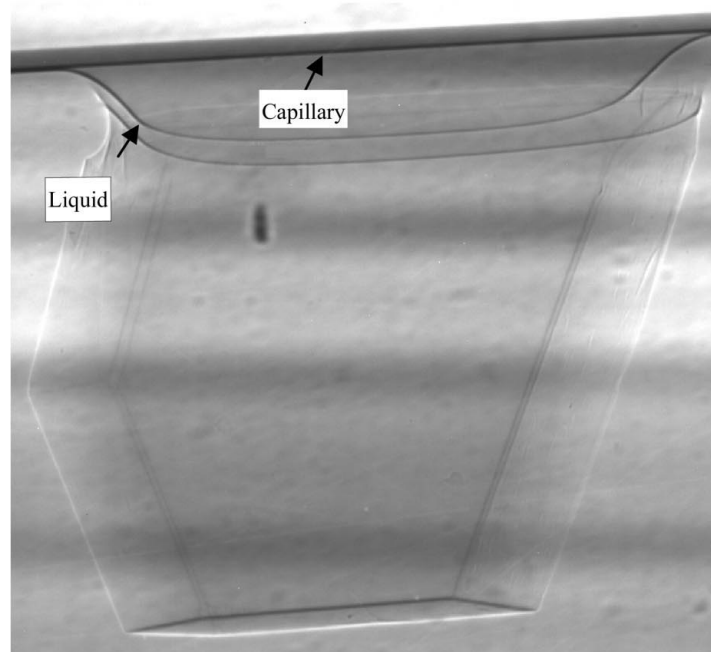
On average, $\theta_{1/2}(1)$ is only of the order of 10^{-1} arcsec or less for protein crystals, in contrast to several arcseconds for most inorganic crystals. Even for crystals of lysozyme (a small protein), $\theta_{1/2}$ is only $\sim$0.3 arcsec for the above 4 4 0 reflection and $\sim$0.02 arcsec for the above 26 0 2 reflection. In other words, a highly collimated incident beam with an angular divergence of few arcseconds or less may not act as a plane wave in effect, depending on the quality of the sample and the
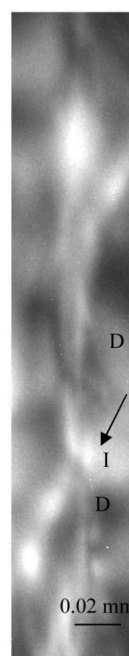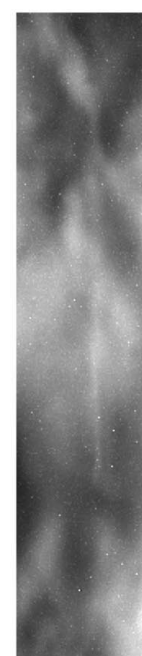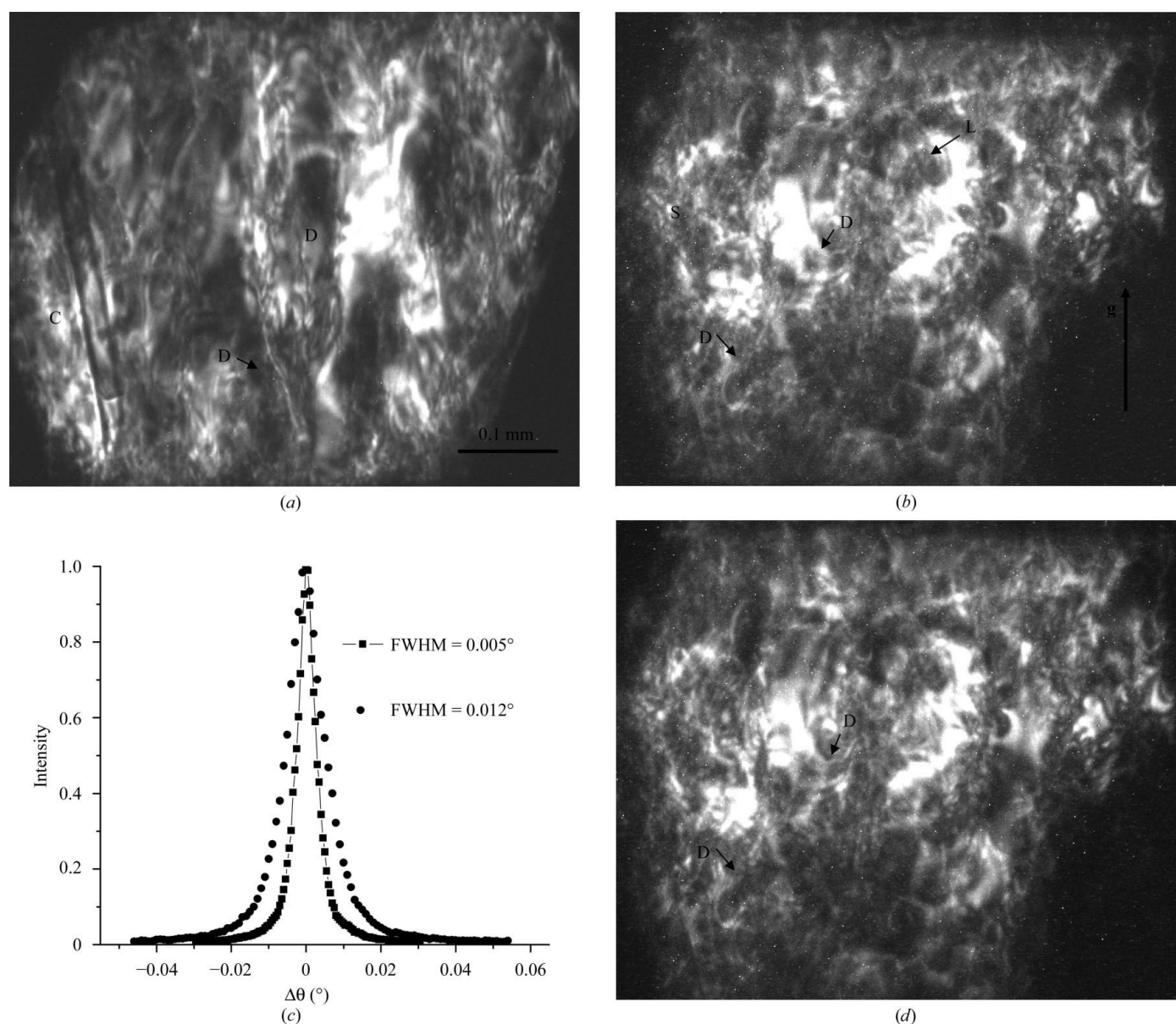

Figure 2
Phase-sensitive X-ray images and a rocking curve of a uniformly grown lysozyme crystal, 4 4 0 reflection. (*a*) Phase-sensitive X-ray diffraction image, $R_d \simeq 10$ cm. (*b*) 4 4 0 rocking curve. (*c*) Phase-sensitive X-ray radiographic image, $R_d \simeq 9$ cm. (*d*) and (*e*) High spatial resolution diffraction images showing individual line defects originating at the crystal center (*d*) and at an outer growth area (*e*). **g** represents the diffraction vector. D represents the dislocations. C is the phase-sensitive image of a fragment of quartz that accidentally dropped inside the capillary and was positioned behind the sample (against the incoming beam direction). Three horizontal black bands in (*c*) originate from the upstream optics.

reflections used. The sensitivity to lattice distortions by orientation contrast is then lower than that in an otherwise plane-wave topograph. Nevertheless, orientation contrast may have been a dominant effect in most X-ray topographs of protein crystals because of the presence of mosaic domains and lattice bending *etc.*

3. Experimental principles and details

Experiments were conducted at the bending-magnet beamline 2BM of X-ray Operation and Research (XOR) at the Advanced Photon Source (APS). The experimental setup is schematically shown in Fig. 1. A double-bounce Si(111) monochromator was employed to deliver an incident beam

with a beam pass ($\Delta\lambda/\lambda$) of $\sim 1.48 \times 10^{-4}$ at a wavelength of ~ 0.95 Å. The effective beam divergence in the vertical scattering plane is $\sim 10^{-5}$ rad. A four-circle diffractometer was used along with a scintillation detector and a lens-coupled high-resolution charge-coupled device (CCD) camera to carry out combined diffraction and imaging experiments. Two modes were applied for spatial coherence-based imaging, mode 1 being the phase-sensitive radiographic imaging mode and mode 2 the phase-sensitive diffraction imaging mode. The first mode is refraction-based and is effective in mapping of the edges of protein crystals, where the gradient of the refractive index is great. This turns out to be useful to examine the integrity of protein crystals and to orientate samples for desired reflections, although bulk protein crystals themselves
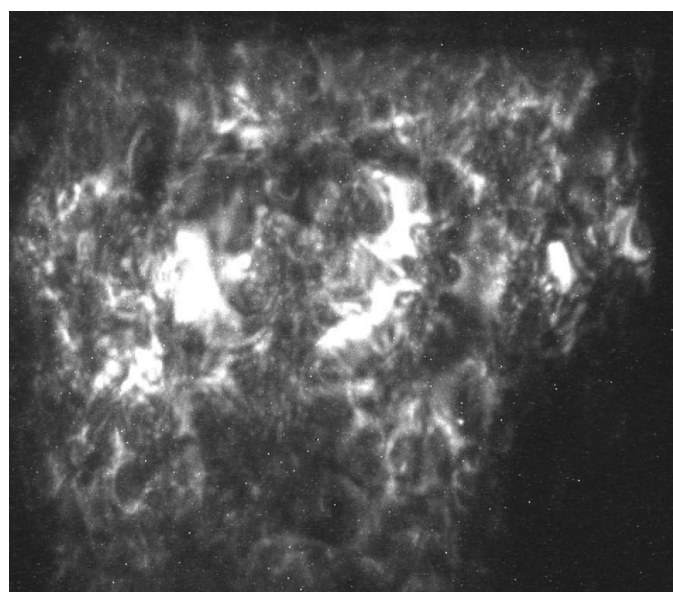

Figure 3
Evolution of defect structures of the lysozyme crystal during dehydration, 4 4 0 reflection, $R_d \simeq 21$ cm. (*a*) and (*b*) were taken at intervals of 3 and 65 h relative to Fig. 2(*a*), respectively. (*c*) 4 4 0 rocking curves. The squares and dots correspond to (*a*) and (*b*), respectively. (*d*), (*e*) and (*f*) are a sequence of images taken at intervals of ~ 12 min, ~ 36 min and ~ 3 h relative to (*b*), respectively. (*g*) 4 4 0 rocking curves. The solid and dotted curves correspond to (*b*) and (*f*), respectively.

are practically transparent to the hard X-rays used. In the second mode, the diffracted beam is invoked for imaging and is used for mapping of defects and/or any phase-related features of protein crystals by incorporating the phase information of the exit wave into X-ray diffraction images. It should be mentioned that wave interactions in free space are usually ignored within the scope of classical X-ray topography, in which only wave interactions within the crystal are taken into account. In conventional X-ray topography, a diffraction topograph recorded immediately after the sample is assumed to be identical to that obtained at a large detector-to-sample distance, except for the difference in spatial resolution caused by a geometric effect. On a rotating-anode X-ray generator with an effective source size of 1×0.5 mm^2 (point focus) and a limited sample-to-source distance, say 1 m, a small sample-to-detector distance (R_d) of between several millimetres and

(e)

10 mm is always desirable for reasonably good spatial resolution. However, with a small source size S (nominally, $S_x = 102$ μm and $S_y = 35$ μm at 3.0 nm rad emittance, where x and y denote the horizontal and vertical directions, respectively) and a large sample-to-source distance ($R_s = 55$ m) at 2BM of the APS (http://www.aps.anl.gov/aps/frame_operations.html), the geometric resolution associated with the source, $R = S(R_d/R_s)$, remains high even if the sample-to-detector distance (R_d) reaches 1 m ($R_x = 1.9$ μm and $R_y = 0.6$ μm if $R_d = 1$ m). At 0.95 Å radiation, the nominal spatial coherence length provided by the source, $\lambda R_s/2S$, is ~75 μm in the vertical direction and ~26 μm in the horizontal direction. With such a coherent X-ray beam, increasing R_d can be considered to be equivalent to defocusing as in electron microscopy (Cowley, 1995) and in X-ray radiography (Snigirev *et al.*, 1995; Cloetens *et al.*, 1996; Wilkins *et al.*, 1996; Nugent *et al.*, 1996) for phase visualization, thus in favorable cases enabling the phase shifts that phase-related defects imprint on the exit wave to be visible in the form of phase contrast in diffraction images (Hu, Lai *et al.*, 2001). By adding the phase-contrast effects to diffraction images or topographs, the contrast of the phase-related defects and/or features of crystals can be augmented in diffraction images.

Hen egg-white lysozyme (HEWL; Seikagaku America, MA, USA) was crystallized without further purification (Thomas *et al.*, 1996, 1998) using a control batch growth at a supersaturation of 35 mg ml^{-1} in 50 mM sodium acetate buffer pH 4.5 with 4% sodium chloride. A well faceted and optically defect-free crystal with a thickness of ~0.35 mm was mounted in a 1.5 mm diameter X-ray quartz capillary with walls of 0.01 mm thickness that was then sealed for experiments. During the first stage of measurements there were two small plugs of mother liquor placed a few millimetres away from the sample at either end of the capillary. After the first-stage measurements, one plug of mother liquor from the top end of
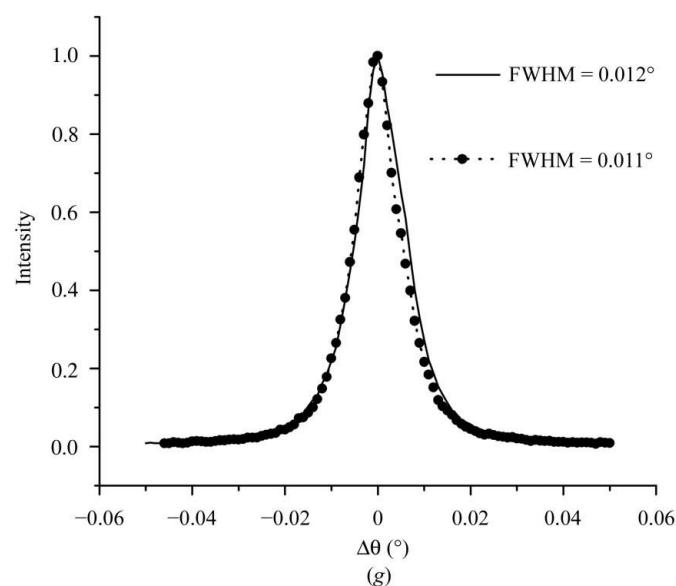
(f)

(g)
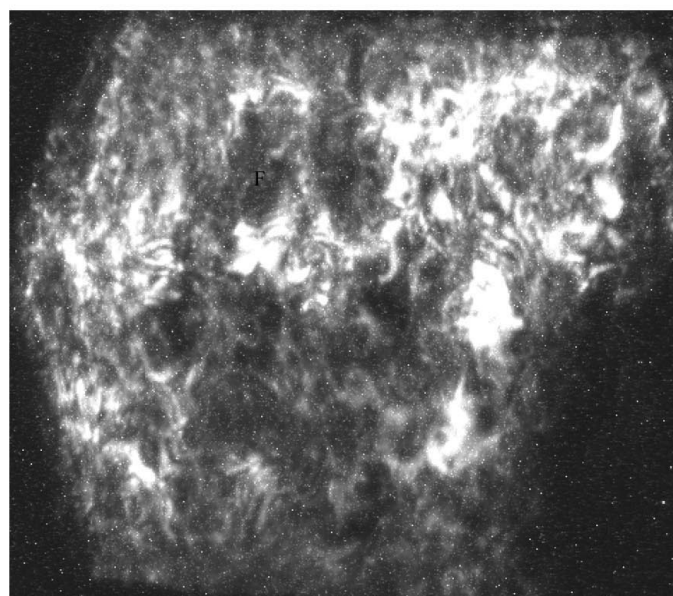
Figure 3 (continued)

the capillary and the mother liquor around the sample was removed. The capillary was then sealed so that slow dehydration of the sample took place. The sample was re-examined to determine how crystal defects respond to the subtle and gradual change of the local environment of the crystal. A 4 4 0 reflection in the symmetric Laue case was selected for diffraction and diffraction-imaging measurements; its extinction length was approximately 2 mm using 0.95 Å radiation.

4. Experimental results

Fig. 2(a) is a phase-sensitive X-ray diffraction image of the uniformly grown HEWL crystal taken with the 4 4 0 reflection, revealing conspicuously non-uniform contrast across the entire sample. Note that the images shown here and below are negatives (i.e. white regions diffract strongly). The corresponding 4 4 0 rocking curve (Fig. 2b) is quite symmetric with respect to angular deviation from the Bragg-angle position and the FWHM is 0.0048°. The entire crystal was completely bathed in the incident beam and hence the FWHM value gives a measure of the 'perfection' of the whole crystal. Fig. 2(c) is a phase-sensitive X-ray radiographic image of the sample in which the well defined contrast features at the sample edges indicate that the sample integrity is fairly well preserved during handling. Among the complicated defect structures shown in Fig. 2(a), one of the major features is vertical lines running roughly parallel to the ⟨1 1 0⟩ growth front. Although a variety of defects and slight lattice bending of the sample combined with the high-angular-sensitivity characteristic of the image somewhat obscure individual defects, the line defects that carry distinct dislocation features are discernable, e.g. marked D in the central region of Fig. 2(a). This can be seen more clearly in Fig. 2(d): an image with high spatial resolution in which the line defects (marked D) generated at a central nucleus are resolved. Diffracted intensity appears strikingly non-uniform across the central nucleus region, where a number of intense spots (e.g. that marked I) which presumably arise from inclusions of impurities or foreign particles are clearly visible. One sees that the dislocation D running upwards extends to the sample surface in Fig. 2(d). Fig. 2(e) shows a clean line defect originating at a outer growth area and running straight towards the sample surface.

The sample was re-examined after the slow dehydration started (see §3) in an attempt to catch a glimpse of how defects respond to the slow drying. Figs. 3(a) and 3(b) show two images taken with an interval of ∼3 and ∼65 h relative to Fig. 2(a), respectively. Note that the sample in Fig. 3(b) is slightly distorted with respect to that in Figs. 2(a) and 3(a) because of dehydration effects. Defect contrast is further enhanced in Fig. 3(a) compared with that in Fig. 2(a), which is partially attributed to the stronger phase-contrast effects generated by increasing the detector-to-sample distance from ∼10 to ∼21 cm. A few line defects in Fig. 3(a) appear to have altered slightly in position or shape compared with those in Fig. 2(a), e.g. the line defect D indicated by an arrow. Most of the line-defect images which are intensely visible around the middle region of Fig. 3(a) have either disappeared or altered

in Fig. 3(b). Furthermore, contrast dots and granular contrast features develop across the sample and in many cases these small spots appear to be of 'microscopic domains' with dimensions of ∼5–10 µm (e.g. that marked S in the far-left part of the sample; Fig. 3b). The images clearly show that lattice disordering and restructuring took place during dehydration. The 4 4 0 rocking curve measured after drying has broadened by a factor of ∼2.6 relative to that measured before drying (Fig. 3c, after making a correction for the instrumental broadening), but remains fairly symmetric. In general, a decrease in the degree of lattice perfection affects the visibility of defects in diffraction images. However, it seems less likely that the measure of deterioration of the crystal quality shown in Fig. 3(c) would be sufficient to make all those original line defects completely invisible in the images. Note that a number of 'new' line defects are discernable, e.g. those marked D and L in Figs. 3(b) and 3(d). This phenomenon suggests that the movement and evolution of line defects occurred during dehydration. This is consistent with the argument that those individual line defects are dislocations, since dislocations are peculiar among defects by their ability to propagate in lattices. Of course, dislocations can remain immobile, for example, by impurity segregation. Loops are also observable and in one case two or more loops coalesce into an elongated foot-shaped loop (marked L in the upper part of Fig. 3b). Figs. 3(d), 3(e) and 3(f) are a sequence of images taken in situ with an interval of ∼12 min, ∼36 min and ∼3 h relative to Fig. 3(b). The overall structural features in Fig. 3(d) and 3(e) appear almost the same as those in Fig. 3(b), yet a slight variation of contrast indicative of local structural change is discernable in some areas. The line defect D at to the left of the center of Fig. 3(d) is more clearly seen than that in Figs. 3(b) and 3(e), forming an L-like shape with two segments running roughly along ⟨1 1 0⟩ and ⟨0 0 1⟩. An appreciable change is observed in Fig. 3(f), where defect rearrangements developed further to reduce dehydration-induced strain energy, but a fringe-like pattern F emerges locally and is probably indicative of a structural change taking place in the local area as a result of water loss. However, the rocking-curve width (Fig. 3g) changed little over time. Rocking curves were sequentially measured to monitor X-ray radiation damage to the crystal. Fig. 4 indicates that no significant change of the 4 4 0 rocking curve took place after an accumulated 3 h X-ray exposure of the sample. The above results show the extreme sensitivity of the imaging method to individual defects (or defects in bundles) and any local structural changes while the overall degree of lattice perfection may or may not change significantly.

5. Discussion

The richness of the observed features offers some insight into the causes of the broadening of the rocking curve, a question that is crucial to understanding how the crystal mosaicity affects the diffraction performance. The FWHM of the 4 4 0 reflection from the original sample (Fig. 2b) is approximately 16.7 arcsec (after making a correction for the instrumental broadening) compared with 0.3 arcsec, the estimated value for

the intrinsic FWHM of the 4 4 0 reflection from a perfect tetragonal lysozyme crystal. The defects observed throughout the crystal, along with lattice bending, contribute significantly to the broadening of the peak width. The extent of molecular disorder caused by the densely distributed defects across the crystal can be greater than that produced by a few large and individually well ordered macroscopic mosaic domains contained in a crystal, although a crystal corresponding to the latter may give a greater rocking-curve width as a result of the macroscopic misorientation generated.

The images of most of the vertical line defects shown in Figs. 2(a), 2(d), 2(e) and 3(a) appear to be of approximately constant width over considerably large distances (after taking the defect-overlapping effect into account). In addition, the majority of the line defects originate at or around the central nucleus and run outward to the crystal surfaces. The observed features suggest that those straight line defects run approximately along the ⟨1 1 0⟩ growth front or parallel to the diffraction vector **g** (Figs. 2a, 2d and 2e). It is more likely that they are growth-induced screw dislocations with a possible Burgers vector **a**⟨1 1 0⟩, which is in agreement with the observation of line defects in an extremely large lysozyme crystal using Laue topography (Izumi *et al.*, 1999). The excessive non-uniform contrast features at and around the central nucleus (Figs. 2a and 2d) may suggest that nucleation is heterogeneous. Foreign particles and the crystallization-plate wall can all act as a substrate for protein crystal growth (Ducruix & Giegé, 1999). Dislocations were then generated by initially faulty growth on the substrate. On the other hand, initial fast growth under the conditions of a highly supersaturated solution that results in homogenous nucleation may be favorable to the formation of dislocations. Because of the high supersaturation, impurities or foreign particles tend to be

readily trapped in lattices during the early stages of growth (Chernov & Komatsu, 1995). The images of the intense dots (marked I in Fig. 2d) at the point of origin may indicate that dislocation nucleation has taken place at inclusions. There are a good number of intense dots in the central growth region, varying from a few micrometres to about 10 μm in size. A 50–100 μm wide region of intensity enhancement associated with an impurity-rich growth core (Vekilov *et al.*, 1996) was observed in the X-ray topographs of specially grown lysozyme crystals (Vekilov *et al.*, 1996; Stojanoff *et al.*, 1997). An individual straight dislocation with ⟨1 1 0⟩ has also been observed in an outer growth region (Fig. 2e) in which imperfect growth probably occurred during crystal growth. A few dislocations appear as 'zigzags' in the images, indicating that they underwent post-growth motion (Klapper, 1991). For example, the line defect D denoted by an arrow (Fig. 2a) contains short bent segments, but shows major straight portions along ⟨1 1 0⟩. The geometric features may imply that this line defect is also a growth-induced screw-type dislocation, bent by glide along [0 0 1] in the slip plane (1 1 0). It appears that the observed evolution of the bent line defect D from Fig. 2(a) to Figs. 3(a) and 3(b) supports this interpretation. In the tetragonal lysozyme form, [0 0 1] is the direction along which the molecules are most closely packed. In addition, [0 0 1] (1 1 0) is one of the common slip systems in the tetragonal system (Friedel, 1964). Given the intrinsically weak macromolecular bonding and the relatively small number of protein–protein contact points on molecular surfaces, it is possible that the strains built up at microscopic stress centers (Chernov, 1999) during crystal growth and the stress induced during post-growth processing could modify and/or generate dislocations *via* plastic deformations. Dislocation loops induced by stress relaxation have been observed in previous work (Hu, Lai *et al.*, 2001). High-angular-resolution triple-axis X-ray reciprocal-space mapping and topographic studies (Hu, Thomas *et al.*, 2001) of acetylated lysozyme-doped lysozyme crystals (Thomas & Chernov, 2001) also indicated that the lattice strains created by the non-uniform uptake of impurities into lattices were largely relaxed by formation of mosaic structures. Similar results were obtained in a comparative study of flight- and earth-grown lysozyme crystals (Boggon *et al.*, 2000).

The ratio of water to protein molecules may vary from one crystal to another. There are approximately 350 water molecules per protein molecule in the tetragonal HEWL crystal form (Kundrot & Richards, 1988), of which about 140 are bound water molecules (Hagler & Moult, 1978; Blake *et al.*, 1983). Drying led to the loss of the 'bulk water' in the lattices and probably to the shrinkage of the channels that were originally filled with the liquid solvent. As visible in the images, the dehydration process occurred inhomogeneously across the crystal: strains were first induced at the interfaces between water-deficient regions and 'virgin areas'. The dehydration-induced strains would be responsible for the dislocation re-arrangements and/or movements, which in turn reduce overall strain energy. The broadening of the peak width measured from the dehydrated crystal (Figs. 2b and 3c) is significant considering the nature of the observed defects in
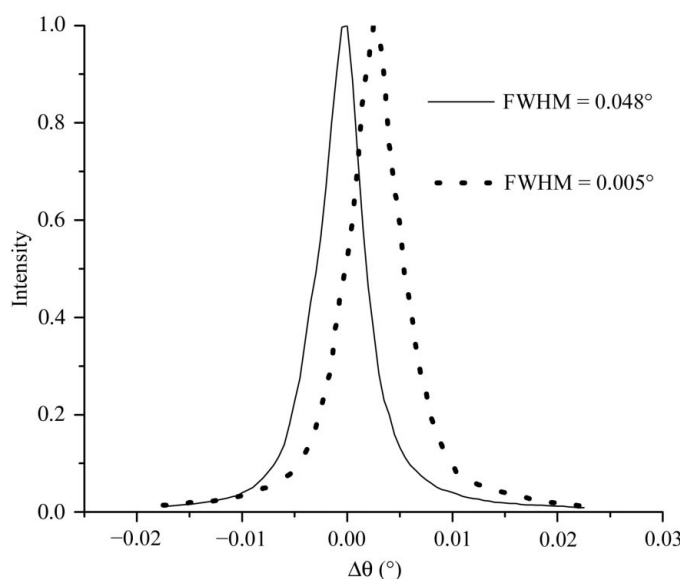
Figure 4
4 4 0 rocking curves measured before (solid line) and after (dotted line) an accumulated X-ray exposure of ∼3 h. The origin of the peak position is deliberately offset for clarity.

the crystal and the Bragg reflection used. The increased width of the rocking curve results primarily from two causes: residual microscopic strains and lattice rotations or misorientations. The fact that no macrocracks or macroscopic misorientations were observed from the topographic images (Figs. 3b, 3d, 3e and 3f) indicates that the crystal was not dried such that the crystal became brittle. It is the microscopic effects that result in a broadening factor of ~2.6 in the width of the rocking curve.

6. Concluding remarks

The demand for high-quality protein crystals continues to grow in the post-genomics era (Chayen & Saridakis, 2002) as well ordered crystals are a prerequisite for determining protein structure by X-ray crystallography. Hence, studies of the quality and defects of biological macromolecular crystals will be of increasing importance in providing the rationale for crystallization of better ordered protein crystals for structural determination and drug design. The importance of X-ray topography in the study of the perfection and properties of protein crystals is obvious because the great penetration of X-rays allows the bulk of protein crystals to be topographically examined. However, given the limited thickness of typical protein crystals, the intrinsically weak X-ray scattering power and hence the long extinction length of protein crystals, it can be difficult to visualize line defects and other microdefects in X-ray topographs. In the present paper, we apply phase-contrast X-ray diffraction imaging and radiographic imaging combined with high-resolution X-ray diffraction measurements to the study of the lattice perfection and defects of a lysozyme crystal and the microstructural response to dehydration. Of great importance is the extreme sensitivity of the coherence-based phase-contrast X-ray imaging techniques that would enable line defects, inclusions and other lattice imperfections in an entire protein crystal to be mapped in the as-grown state. The information revealed about individual line defects, inclusions and/or other microdefects, the spatial distribution of the defects and the microstructural change with drying, along with high-quality rocking-curve measurements under well defined diffraction geometry, has shed light not only on the crystal perfection and/or quality in general, but also on the nature and formation of defects and crystal nucleation and properties. Continued improvement in the experimental setup and the CCD detector technology would enable complete sets of images of a crystal to be acquired prior to appreciable radiation damage occurring to the crystal, which would allow the nature and behavior of defects to be studied in a more conclusive manner. With a highly coherent X-ray source and an algorithm for phase retrieval, it would even be possible to obtain the complete information on a defect from one single phase-imaging pattern under certain conditions. By taking one step further, we can conduct in situ X-ray diffraction imaging studies of protein crystal growth under carefully designed crystallization conditions, which would yield new insights into the origins of defect formation and growth mechanisms.

References

Authier, A. (2001). *Dynamical Theory of X-ray Diffraction*. Oxford University Press.
Blake, C. C. F., Pulford, W. C. A. & Artymiuk, P. J. (1983). *J. Mol. Biol.* **167**, 693–723.
Boggon, T. J., Helliwell, J. R., Judge, R. A., Olczak, A., Siddons, D. P., Snell, E. H. & Stojanoff, V. (2000). *Acta Cryst.* D**56**, 868–880.
Chayen, N. E. (2002). Am. Crystallogr. Assoc. Ann. Meet. Abstr., p. 76.
Chayen, N. E. & Saridakis, E. (2002). *Acta Cryst.* D**58**, 921–927.
Chernov, A. A. (1999). *J. Cryst. Growth*, **196**, 524–534.
Chernov, A. A. & Komatsu, H. (1995). *Science and Technology of Crystal Growth*, edited by O. S. L. Bruinsma & J. P. van der Eerden, pp. 329–350. Dordrecht: Kluwer Academic Press.
Cloetens, P., Barret, R., Baruchel, J. & Guigay, J. P. & Schlenker, M. (1996). *J. Phys. D*, **29**, 133–146.
Cowley, J. M. (1995). *Diffraction Physics*, 3rd ed. Amsterdam: North-Holland.
Dobrianov, I., Kriminski, S., Caylor, C. L., Lemay, S. G., Kimmer, C., Kisselev, A., Finkelstein, K. D. & Thorne, R. E. (2001). *Acta Cryst.* D**57**, 61–68.
Ducruix, A. & Giegé, R. (1999). *Crystallization of Nucleic Acids and Proteins*. Oxford University Press.
Fourme, R., Ducruix, A., Riès-Kautt, M. & Capelle, B. (1995). *J. Synchrotron Rad.* **2**, 136–142.
Friedel, J. (1964). *Dislocations*. Oxford: Pergamon.
Garman, E. (1999). *Acta Cryst.* D**55**, 1641–1653.
Garman, E. F. & Schneider, T. R. (1997). *J. Appl. Cryst.* **30**, 211–237.
Hagler, A. T. & Moult, J. (1978). *Nature (London)*, **272**, 222–226.
Helliwell, J. R. (1988). *J. Cryst. Growth*, **90**, 259–272.
Hu, Z. W., Lai, B., Cai, Z., Chu, Y. S., Mancini, D. C., Thomas, B. R. & Chernov, A. A. (2001). *Phys. Rev. Lett.* **87**, 148101–1–148101–4.
Hu, Z. W., Thomas, B. R. & Chernov, A. A. (2001). *Acta Cryst.* D**57**, 840–846.
Hu, Z. W., Thomas, P. A., Snigirev, A., Snigireva, I., Sourorov, A., Smith, P. G. R., Ross, G. W. & Teat, S. (1998). *Nature (London)*, **392**, 690–693.
Izumi, K., Taguchi, K., Kobayashi, Y., Tachibana, M., Kojima, K. & Ataka, M. (1999). *J. Cryst. Growth*, **206**, 155–158.
Klapper, H. (1991). *Crystals: Growth, Properties and Applications*, Vol. 13, pp. 109–162. Berlin: Springer-Verlag.
Kundrot, C. E. & Richards, F. M. (1988). *J. Mol. Biol.* **200**, 401–410.
Lang, A. R. (1978). *Modern Diffraction and Imaging Techniques in Materials Science*, Vol. II, edited by S. Amelincx, R. Gevers & J. van Landuyt, pp. 623–714. Amsterdam: North Holland.
Lim, K., Nadarajah, A., Forsythe, E. L. & Pusey, M. L. (1998). *Acta Cryst.* D**54**, 899–904.
McPherson, A. (1998). *Crystallization of Biological Macromolecules*. Cold Spring Harbor, NY, USA: Cold Spring Harbor Laboratory Press.
Matthews, B. W. (1968). *J. Mol. Biol.* **33**, 491–497.
Morozov, V. N., Morozova, T. Ya., Myachin, E. G. & Kachalova, G. S. (1985). *Acta Cryst.* B**41**, 202–205.
Nugent, K. A., Gureyev, T. E., Cookson, D. F., Paganin, D. & Barnea, Z. (1996). *Phys. Rev. Lett.* **77**, 2961–2964.
Otalora, F., Garcia-Ruiz, J. M., Gavira, J. A. & Capelle, B. (1999). *J. Cryst. Growth*, **196**, 546–558.
Perutz, M. F. (1942). *Nature (London)*, **149**, 491–494.

Salunke, D. M., Veerapandian, B., Kodandapani, R. & Vijayan, M. (1985). *Acta Cryst.* B**41**, 431–436.

Snigirev, A., Snigireva, I., Kohn, V., Kuznetsov, S. & Schelokov, I. (1995). *Rev. Sci. Instrum.* **66**, 5486–5492.

Stojanoff, V., Siddons, D. P., Monaco, L. A., Vekilov, P. & Rosenberger, F. (1997). *Acta Cryst.* D**53**, 588–595.

Tanner, B. K. (1976). *X-ray Diffraction Topography*. Oxford: Pergamon.

Thomas, B. R. & Chernov, A. A. (2001). *J. Cryst. Growth*, **232**, 237–243.

Thomas, B. R., Vekilov, P. G. & Rosenberger, F. (1996). *Acta Cryst.* D**52**, 776–784.

Thomas, B. R., Vekilov, P. G. & Rosenberger, F. (1998). *Acta Cryst.* D**54**, 226–236.

Vekilov, P. G., Monaco, L. A., Thomas, B. R., Stojanoff, V. & Rosenberger, F. (1996). *Acta Cryst.* D**52**, 785–798.

Vetter, W. M., Gallagher, D. T. & Dudley, M. (2002). *Acta Cryst.* D**58**, 579–584.

Wilkins, S. W., Gureyev, T. E., Gao, D., Pogany, A. & Stevenson, A. W. (1996). *Nature (London)*, **384**, 335–338.